Theor Chem Acc (2005) 114: 52–59
DOI 10.1007/s00214-005-0643-2

REGULAR ARTICLE

**Thomas Bredow · Gianfranco Pacchioni**

# NO adsorption on the stoichiometric and reduced $SnO_2$(110) surface

Received: 30 August 2004 / Accepted: 17 November 2004 / Published Online: 13 May 2005


**Abstract** The adsorption of NO molecules on the perfect and defective (110) surfaces of $SnO_2$ was studied with first-principles methods at the density-functional theory level. It was found that NO mainly interacts via the nitrogen atom with the bridging oxygens of the stoichiometric surface while the coordinatively unsaturated surface Sn atoms are less reactive. On the oxygen-deficient surface, NO is preferentially adsorbed at the vacancy positions, with the nitrogen atom close to the former surface oxygen site. Regardless of the adsorption site, the unpaired electron is located mainly on the NO molecule and only partly on surface Sn atoms. The results for the $SnO_2$ surface are compared to literature results on the isostructural $TiO_2$ rutile (110) surface.

**Keywords** Tin dioxide surface · NO adsorption · Density-functional methods

## 1 Introduction

Tin dioxide $SnO_2$ has a rutile structure. Similar as in the isostructural oxides $TiO_2$ and $RuO_2$, the most stable surface is the (110) crystallographic plane. The surface morphology of $SnO_2$(110) has been reviewed recently [1].

The material is of high technological importance due to its use as gas sensor, catalyst, and as varistor [2–4]. The gas-kinetic interaction of nitrous oxides, NO, and $NO_2$ with $SnO_2$ surfaces has been investigated experimentally [5]. The nature of adsorbed $NO_x$ species on $SnO_2$-based sensors has been investigated with temperature programmed desorption (TPD) and diffuse reflectance spectroscopy [6]. Four types of adsorbates of NO on $SnO_2$ surfaces were recognized in a combined measurement of electrical resistance and TPD [7], a cationic dimer, two forms of nitrosyls bound to surface tin atoms, and a nitrite Sn–O–NO-species. The relative abundance of the latter three species was found to be affected by the presence of oxygen vacancies. In a recent study of ammonia adsorption, it was found that low-coordinated Sn sites at bridging oxygen vacancies are more reactive towards $NH_3$ than fivefold coordinated Sn sites on the regular surface [8].

In an experimental study of NO adsorption on the isostructural $RuO_2$(110) surface [9], it was found that at a small dosage adsorption takes place at fivefold coordinated Ru sites with an almost linear Ru–N–O bond. The NO desorption enthalpy was measured as 1.16–1.34 eV. At a higher dosage, NO was also attached to the bridging oxygens forming $NO_2$ species.

Recently, a DFT study of the NO adsorption on the regular and defective (110) surface of $TiO_2$ rutile has been performed [10]. It was found that the nondefective surface is not very reactive towards NO. At the fivefold coordinated surface Ti atoms, adsorption energies of 0.35 eV (N-down) and 0.18 eV (O-down) were obtained at coverage $\theta = 0.5$. The interaction energy was considerably increased, up to 1.59 eV, when oxygen vacancies were present on the surface.

There exists a number of theoretical studies on the $SnO_2$(110) surface [11–25]. They are mainly related to the surface geometrical and electronic structure [12, 15–17, 20, 23], the formation of oxygen vacancies [11, 18, 21, 24], or the adsorption of molecules like $H_2O$ [13, 25], methanol [14], and oxygen [22, 24]. To our knowledge, the present study is the first one that addresses the adsorption of NO at the $SnO_2$ surface.

We have performed first-principles periodic calculations to analyze the NO–$SnO_2$ interaction, to locate the preferred adsorption sites and adsorption geometries as a function of the coverage. The effect of surface defects, such as oxygen vacancies, has also been considered.

Dedicated to Professor Karl Jug on the occasion of his 65th birthday

T. Bredow (✉)
Theoretische Chemie, Universität Hannover,
Am Kleinen Felde 30, 30167 Hannover, Germany
E-mail: bredow@mbox.theochem.uni-hannover.de

G. Pacchioni
Dipartimento di Scienza dei Materiali,
Università di Milano-Bicocca, via R. Cozzi 53, 20125 Milano, Italy

**Table 1** Optimized valence basis set for Sn; the inner 1s-4spd shells are replaced by the Hay-Wadt effective core potential [31,32]

| Shell | Exponent | Coefficients | |
|---|---|---|---|
| | | s | p,d |
| 5sp | 1.0470 | 0.016 | −0.133 |
| | 0.5418 | −0.681 | −0.028 |
| | 0.3784 | 0.732 | 0.005 |
| | 0.1932 | −0.008 | 0.991 |
| 6sp | 0.0926 | 1.000 | 1.000 |
| 5d | 0.1860 | | 1.000 |

**Table 2** Lattice parameters $a$, $c$ (Å), fractional coordinate $u$, bulk modulus $B$ (GPa), atomization energy $E_a$ (eV) for bulk $SnO_2$

| Method | Program | $a$ | $c$ | $u$ | $B$ | $E_a$ |
|---|---|---|---|---|---|---|
| PW-GGA | CRYSTAL03 | 4.724 | 3.182 | 0.307 | 185 | 15.57 |
| HFPW | CRYSTAL03 | 4.683 | 3.154 | 0.307 | 210 | 14.99 |
| PW-GGA | VASP | 4.737 | 3.190 | 0.306 | 219 | 17.80 |
| B3LYP[a] | CRYSTAL98 | 4.718 | 3.187 | 0.307 | | |
| PW-GGA[b] | VASP | 4.778 | 3.232 | 0.306 | | |
| Exp. | | 4.737[c] | 3.186[c] | 0.307[c] | 205[c] | 14.27[d] |

[a]Ref. [24]
[b]Previous VASP study using Vanderbilt ultrasoft pseudopotentials [20]
[c]Ref. [36]
[d]Ref. [37]

## 2 Computational methods and surface models

### 2.1 Computational methods

Two different methods were employed in the present study. The structure optimizations were performed mainly with the plane-wave code VASP [26]. Different from earlier applications [20–23] on $SnO_2$ where inner electrons were replaced by Vanderbilt ultrasoft pseudopotentials (USP) [27], the projector-augmented wave (PAW) approach [28,29] was used here. In all calculations, an energy cut-off value of 396 eV was used. Geometry optimizations were assumed to be converged when the gradients were smaller than 0.03 eV/Å. No symmetry restrictions were applied. In the electronic structure calculations, a Gaussian smearing with a half-width $\sigma$ of 0.2 eV was used.

Surface relaxation and selected adsorption structures were calculated also with the crystalline orbital program CRYSTAL03 [30]. In the CRYSTAL03 calculations, the inner $1s^2$ to $4s^24p^64d^{10}$ electrons of Sn are replaced by an effective core potential of Hay and Wadt [31]. The valence electrons are described with a modified double-zeta plus polarization basis derived from that generated by Check et al. [32]. The orbital exponents and contraction coefficients optimized for bulk $SnO_2$ at experimental geometry are shown in Table 1. Oxygen atoms are described with an all-electron 8-411G* basis set [33].

The gradient-corrected functional by Perdew and Wang (PW–GGA) [34] was used for the adsorption studies. This functional has been applied in previous studies of $SnO_2$ surfaces [20]. Analysis of the electronic structure was performed in selected cases also with a hybrid method, where the exchange functional has 20% contribution of the exact Hartree–Fock expression and 80% of the PW–GGA functional. This hybrid approach, referred to as HFPW in the following, has already been applied to other metal oxides [35].

### 2.2 Surface models

In the plane-wave formalism, the surface is treated as a quasi three-dimensional system with a vacuum separation between the slabs. The size of the separation affects the accuracy of the simulation. The convergence of calculated properties with increasing vacuum thickness has to be checked. In the present study, we used a vacuum width of 10 Å, a value that has been shown to be sufficient for adsorption studies on the $SnO_2$(110) surface [20–23]. In CRYSTAL03, two-dimensional periodic boundary conditions are applied to the basic unit and no vacuum width has to be specified.

For the adsorption studies, the $SnO_2$(110) surface was described with primitive (1×1) surface unit cells, and with (2×1) and (3×1) supercells in order to simulate lower coverages, $\theta = 0.5$ and $\theta = 0.33$, respectively.

The number of stoichiometric $SnO_2$ layers was restricted to three. In the following, the corresponding supercells are denoted as $n \times 1 \times 3$. In previous adsorption studies, models with three to four layers were shown to give reasonably well-converged results with respect to the slab thickness [20–22].

A 2×4 Monkhorst-Pack $k$ point mesh has been used for slab calculations using a primitive unit cell, and a reduced 2×2 mesh was applied to the supercell calculations.

## 3 Results and discussion

### 3.1 Method test: bulk and surface properties

In order to test the methods employed in the present study, the bulk properties of $SnO_2$ were calculated and compared to experimental data from the literature and to previous calculations (Table 2). The PW-GGA functional provides an excellent description of the lattice parameters $a$, $c$, and $u$. The computed values, 4.737 Å, 3.190 Å, and 0.306 (VASP) and 4.724 Å, 3.182 Å, and 0.307 (CRYSTAL) deviate by less than 0.3% from the experimental values, 4.737 Å, 3.186 Å, and 0.307 [36]. The differences between CRYSTAL03 and VASP are due to the different basis sets used in the two methods. Interestingly, the agreement of the present PW–GGA–PAW results with the experiment is considerably better than that of a previous VASP study using ultrasoft Vanderbilt pseudopotentials (USP) [20], $a = 4.778$, $b = 3.232$, and $u = 0.306$. Thus, one can expect that the PAW approach describes structural properties with a higher accuracy than the USP approach. For comparison, results of a recent CRYSTAL study using the hybrid method B3LYP [24] are also given in Table 2. The lattice parameters obtained there are quite similar to the present ones.

**Table 3** Relaxation energy $E_r$, surface energy $E_s$ (J/m$^2$), and atomic displacements $\Delta z$, $\Delta y$ with respect to the corresponding bulk positions (Å) for slab models of $SnO_2$(110) with increasing number $N$ of stoichiometric layers

| Method | $N$ | $E_r$ | $E_s$ | $\Delta z(O_{2c})$ | $\Delta z(O_{3c,s})$ | $\Delta y(O_{3c,s})$ | $\Delta z(Sn_{6c})$ | $\Delta z(Sn_{5c})$ | $\Delta z(O_{3c,b})$ |
|---|---|---|---|---|---|---|---|---|---|
| PW-GGA[a] | 3 | −0.38 | 1.37 | +0.02 | +0.17 | −0.06 | +0.17 | −0.08 | +0.00 |
| | 4 | −0.46 | 1.29 | +0.11 | +0.13 | −0.06 | +0.26 | −0.17 | +0.09 |
| | 5 | −0.42 | 1.33 | +0.06 | +0.15 | −0.06 | +0.21 | −0.12 | +0.04 |
| | 6 | −0.44 | 1.32 | +0.08 | +0.14 | −0.06 | +0.23 | −0.14 | +0.07 |
| PW1PW[a] | 3 | −0.97 | 1.58 | +0.01 | +0.15 | −0.06 | +0.17 | −0.09 | +0.00 |
| | 4 | −0.56 | 1.49 | +0.09 | +0.11 | −0.06 | +0.25 | −0.18 | +0.08 |
| | 5 | −0.51 | 1.54 | +0.04 | +0.13 | −0.06 | +0.20 | −0.13 | +0.03 |
| PW-GGA[b] | 3 | −0.32 | 1.46 | +0.02 | +0.17 | −0.06 | +0.14 | −0.07 | +0.00 |
| | 3(2) | −0.16 | | +0.03 | +0.16 | −0.05 | +0.14 | −0.11 | +0.02 |
| | 4 | −0.39 | 1.39 | +0.11 | +0.13 | −0.05 | +0.24 | −0.16 | +0.10 |
| | 5 | −0.36 | 1.42 | +0.05 | +0.16 | −0.05 | +0.18 | −0.10 | +0.04 |
| | 6 | −0.37 | 1.40 | +0.08 | +0.14 | −0.05 | +0.21 | −0.14 | +0.07 |
| B3LYP[c] | 3 | | | +0.00 | +0.11 | | +0.12 | −0.07 | |
| PW-GGA[d] | 6 | | 1.04 | +0.09 | +0.18 | −0.06 | +0.22 | −0.11 | +0.07 |

[a]Present CRYSTAL03 results
[b]Present VASP results
[c]Previous CRYSTAL98 results [24]
[d]Previous VASP results using Vanderbilt ultrasoft pseudopotentials [20,21]

The agreement for the lattice atomization energy is less satisfactory (Table 2). With both codes, the PW–GGA functional considerably overestimates the experimental heat of atomization $\Delta_a H$, 14.27 eV [37], defined with respect to the free gas-phase atoms. While CRYSTAL03 gives a value of 15.57 eV, $\Delta_a H$=17.80 eV is obtained with VASP. This large overestimation can be due to difficulties in converging the atomic references where large cut-off energies and interatomic separations are necessary. For the isolated $^3$O and $^3$Sn atoms, we have used a cut-off energy of 1000 eV, cubic unit cell parameters of 10 Å, and a reduced broadening of 0.1 eV. For this property, the HFPW hybrid performs considerably better than PW–GGA with a value of 14.99 eV for $\Delta_a H$.

The experimental value of the bulk modulus $B$, 205 GPa [36], is overestimated with VASP (219 GPa) and underestimated with CRYSTAL03 (185 GPa); Table 2. This pronounced difference for the two codes using the same functional shows how delicate the calculation of second derivatives is. Numerical accuracy may play a crucial role.

The surface structure of $SnO_2$(110) has been studied with slab models having 3 to 6 stoichiometric layers (Table 3). Different from what has been found for the isostructural $TiO_2$(110) surface [38–41], all computed surface properties converge rather fast with increasing number of layers in the slab models. Already the smallest three-layer model provides results for the relaxation energy $E_r$, the surface energy $E_s$, and atomic displacements $\Delta z$, $\Delta y$ with respect to the corresponding bulk positions which are reasonably close to those obtained with the six-layer model (Table 3). This holds for both implementations of PW–GGA in CRYSTAL03 and VASP, and also for the hybrid functional HFPW, indicating that the convergence is an intrinsic property of the main group oxide and is not affected by the choice of the basis set or the functional. The results from the three-layer model are closer to those from larger slabs when the bottom layer is fixed and only the first two layers are relaxed (entry 3(2) in Table 3).

With the six-layer slab model, the computed surface energy $E_s$ with VASP PAW is 1.40 J/m$^2$. This is considerably larger than the VASP USP PW–GGA value obtained in a previous study, 1.04 J/m$^2$ [21], but relatively close to the present CRYSTAL03 PW–GGA result, 1.32 J/m$^2$. Again, this can be related to the different treatment of inner electrons in the VASP PAW and USP approaches. In general, the energetical and structural properties of $SnO_2$(110) obtained with VASP PAW and CRYSTAL03 are very close. This gives some confidence that spurious effects due to the treatment of inner electrons (VASP) or the incompleteness of the basis set (CRYSTAL) play a minor role in the present study. The displacements of the first-layer atoms, $\Delta z(O_{2c})$, $\Delta z(O_{3c,s})$, $\Delta y(O_{3c,s})$, $\Delta z(Sn_{6c})$, $\Delta z(Sn_{5c})$, and $\Delta z(O_{3c,b})$ are +0.08 Å, +0.14 Å, −0.06 Å, +0.23 Å, −0.14 Å, and +0.07 Å, respectively (VASP results). This agrees with previous DFT

**Table 4** Adsorption and interaction energies $E_{ads}$, $E_{int}$, (eV), and geometries $R, \alpha$ (Å,degrees) for NO monolayers (1×1×3 slab, $\theta = 1$) on the regular $SnO_2$(110) surface; the labels correspond to Fig. 1

| Surface site | Orientation | $E_{ads}$ | $E_{int}$ | Geometries |
|---|---|---|---|---|
| $Sn_{5c}$ | NO (a) | −0.60 | −0.38 | $R_{SnN} = 2.48$, $R_{NO} = 1.16$ $\alpha_{SnNO} = 179$ |
| $O_{2c}$ | NO (c) | −0.85 | −0.63 | $R_{O_{2c}N} = 1.94$, $R_{NO} = 1.16$ $\alpha_{O_{2c}NO} = 107$ |
| $O_{2c}$,$Sn_{5c}$ | O-NO-Sn (d) | −1.03 | −0.81 | $R_{O_{2c}N} = 1.52$, $R_{NO} = 1.25$ |
| | | −1.18[a] | −0.96[a] | $R_{SnO} = 2.27$ $\alpha_{O_{2c}NO} = 112$ |
| $Sn_{5c}$ | ON | −0.43 | −0.21 | $R_{SnO} = 2.60$, $R_{NO} = 1.16$ $\alpha_{SnON} = 179$ |
| $O_{2c}$ | ON | −0.43 | −0.22 | $R_{O_{2c}O} = 2.52$, $R_{NO} = 1.33$ $\alpha_{O_{2c}NO} = 88$ |
| $O_{3c}$ | NO | −0.51 | −0.30 | $R_{O_{3c}N} = 2.76$, $R_{NO} = 1.15$ $\alpha_{O_{3c}NO} = 166$ |
| $O_{3c}$ | ON | −0.35 | −0.14 | $R_{O_{3c}O} = 2.61$, $R_{NO} = 1.15$ $\alpha_{O_{3c}NO} = 148$ |

[a]Obtained with PW-GGA at ROKS level

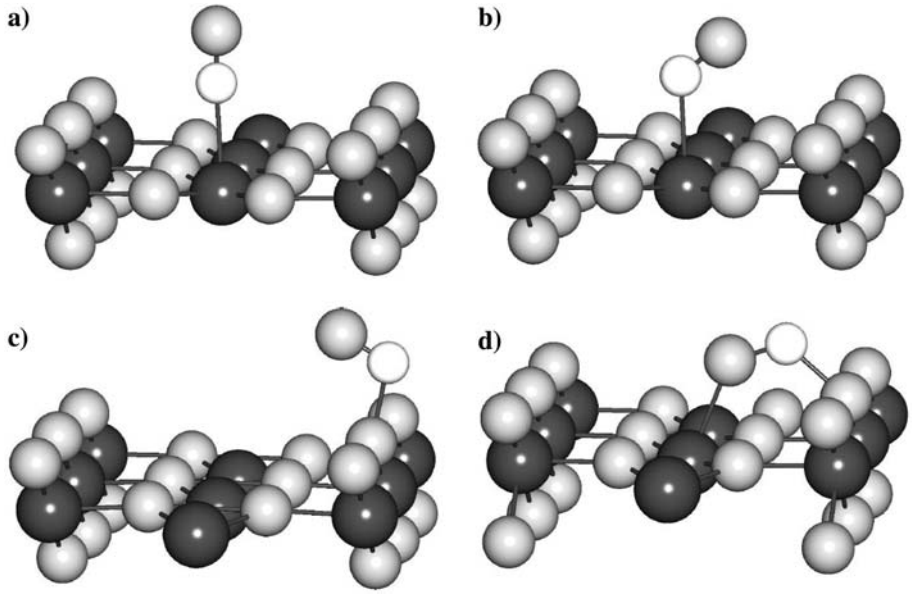


**Fig. 1** NO adsorption structures on the perfect $SnO_2(110)$ surface; *white spheres*: N, *gray spheres*: O, *dark spheres*: Sn

calculations [20, 21] and with the CRYSTAL03 results (Table 3). In particular, the outward movement of the bridging oxygens $\Delta z(O_{2c})$ is different from what is found theoretically and experimentally for $TiO_2$ rutile(110) [42].

## 3.2 NO adsorption

The interaction of NO with the substrate is the first step in catalytic reactions, like disproportionation into $N_2$ and $O_2$ or the formation of other $N_xO_y$ species. Here, we have considered only the NO adsorption and the molecules are treated as isolated even at higher coverage. In a later study, we also plan to investigate NO reactivity. As a first step, we compared the interaction of NO with the stoichiometric and non-stoichiometric $SnO_2(110)$ surface with oxygen vacancies.

### *3.2.1 Stoichiometric $SnO_2(110)$ surface*

The $SnO_2$ surface offers three possible adsorption sites, (a) the coordinatively unsaturated $Sn_{5c}$ atoms, the bridging $O_{2c}$ atoms, and the $O_{3c}$ atoms in the $Sn_{5c}$ plane. NO can interact with the nitrogen or the oxygen atoms to the surface. There is also the possibility of bridging configurations. In order to explore the various possibilities of NO-surface interaction, we employed a rather small surface model, a three-layer $SnO_2$ slab with a primitive $1\times1$ surface unit cell. Thus, in this model the NO coverage corresponds to $\theta = 1$ with respect to one adsorption site. The results obtained with VASP–PAW are summarized in Table 4. The most stable configurations are shown in Fig. 1. For this high coverage, the smallest distance between the NO molecules is relatively short, $\approx 3$ Å. In order to differentiate between lateral NO–NO and NO-surface interaction, we calculated the stabilization energy of unsupported "NO slabs", periodic arrangements of NO molecules in the same configurations as on the surface. For all configurations, a stabilization of 0.21–0.22 eV with respect to the isolated molecule was found. This is contrary to the usual finding that the unsupported layer of adsorbed molecules is less stable than the isolated units because of repulsive intermolecular interactions at short distances. The stabilization in the unsupported NO slab occurs because in the gas-phase the $(NO)_2$ dimer in a singlet state is slightly more stable than two isolated NO molecules [44]. In the unsupported NO slab, this results in a weak bonding between neighboring NO molecules. The stabilization is similar for the different configurations because NO is always parallelly oriented along the [001] direction. The intermolecular distances in this direction are much shorter than in [110] direction. Table 4 therefore contains two values for the binding energy of NO to the surface. $E_{ads}$ is calculated with respect to the free molecule, and $E_{int}$ with respect to the NO slab with corresponding geometry, giving a better approximation of the NO interaction strength with the surface atoms. For most sites, the binding of NO to the perfect (110) surface is rather weak, indicating only physisorption. The strongest interaction ($E_{int} = -0.81$ eV) was obtained for a bridging configuration (Fig. 1d), where the N atom of NO is bound to a $O_{2c}$ surface atom and the oxygen is bent down towards the nearest $Sn_{5c}$ atom. This interaction energy is close to the sum of the separate interaction energies for the $Sn_{5c}$-ON ($-0.21$ eV) and the $O_{2c}$-NO ($-0.63$ eV) configurations. In general, the interaction via the N atom is stronger than via the O atom of NO. The $Sn_{5c}$ atoms bind relatively weakly to NO ($E_{int} = -0.39$ eV) with a rather long Sn–N bond, 2.48 Å. The weak interaction with the surface is also indicated by the small increase in the intermolecular N–O distance, $R_{NO} = 1.16$ Å, compared to the computed

**Table 5** Adsorption energies $E_{ads}$ (eV), and geometries $R, \alpha$ (Å, degrees) for NO submonolayers (2×1×3 supercell, $\theta = 0.5$) on the stoichiometric $SnO_2(110)$ surface; the labels correspond to Fig. 1

| Surface site | Orientation | $E_{ads}$ | Geometries |
|---|---|---|---|
| $Sn_{5c}$ | NO (a) | −0.48 | $R_{SnN} = 2.48$, $R_{NO} = 1.15$ $\alpha_{SnNO} = 174$ |
| $Sn_{5c}$ | NO[a] (a) | −0.50 | $R_{SnN} = 2.42$, $R_{NO} = 1.15$ $\alpha_{SnNO} = 166$ |
| $Sn_{5c}$ | NO (b) | −0.62 | $R_{SnN} = 2.46$, $R_{NO} = 1.15$ $\alpha_{SnNO} = 130$ |
| $O_{2c}$ | NO (c) | −1.02 | $R_{O_{2c}N} = 1.79$, $R_{NO} = 1.15$ $\alpha_{O_{2c}NO} = 109$ |
| $O_{2c}$,$Sn_{5c}$ | O-NO-Sn (d) | −1.23 | $R_{O_{2c}N} = 1.38$, $R_{NO} = 1.25$ $R_{SnO} = 2.23$, $\alpha_{O_{2c}NO} = 115$ |

[a]Adsorption on both sides of the slab model

**Table 6** Adsorption energies $E_{ads}$ (eV), and geometries $R, \alpha$ (Å, degrees) for NO submonolayers (3×1×3 supercell, $\theta = 0.33$) on the stoichiometric $SnO_2(110)$ surface; the labels correspond to Fig. 1

| Surface site | Orientation | $E_{ads}$ | geometries |
|---|---|---|---|
| $Sn_{5c}$ | NO (b) | −0.69 | $R_{SnN} = 2.42$, $R_{NO} = 1.15$ $\alpha_{SnNO} = 128$ |
| $O_{2c}$ | NO (c) | −1.14 | $R_{O_{2c}N} = 1.74$, $R_{NO} = 1.15$ $\alpha_{O_{2c}NO} = 109$ |
| $O_{2c}$,$Sn_{5c}$ | O-NO-Sn (d) | −1.43 | $R_{O_{2c}N} = 1.35$, $R_{NO} = 1.25$ $R_{SnO} = 2.24$, $\alpha_{O_{2c}NO} = 115$ |

**Table 7** Oxygen defect formation energies $E_{def}$ (eV)[a] on the $SnO_2(110)$ surface; *S* singlet state, *T* triplet state; VASP PW–GGA results

| Surface site | Supercell | State | $E_{def}$ |
|---|---|---|---|
| $O_{2c}$ | 2×1×3 | S | 2.95 (2.60[b],3.58[c]) |
| $O_{2c}$ | 2×1×3 | T | 3.59 |
| $O_{2c}$ | 3×1×3 | S | 3.03 |
| $O_{2c}$ | 3×1×3 | T | 3.53 |
| $O_{3c}$ | 2×1×3 | S | 3.76 (3.13[b],3.98[c]) |
| $O_{3c}$ | 2×1×3 | T | 4.65 |
| $O_{3c}$ | 3×1×3 | S | 3.43 |

[a]Reference $\frac{1}{2}E(O_2)$
[b]Previous VASP calculations using Vanderbilt ultrasoft pseudopotentials [20]
[c]present CRYSTAL03 results using the PW–GGA functional

gas-phase value, 1.15 Å. Only for the bridging configuration, $R_{NO}$ is increased to 1.25 Å.

Only the three most stable configurations were selected for calculations of smaller coverages, $\theta = 0.5$ and $\theta = 0.33$ (Tables 5 and 6). For these smaller coverages, the lateral NO-NO interaction becomes negligible and therefore $E_{int}$ is identical to $E_{ads}$. At $\theta = 0.5$, the adsorption energies for all sites are increased considerably compared to $\theta = 1$. For the $Sn_{5c}$-NO, $O_{2c}$-NO, and $O_{2c}$-NO-$Sn_{5c}$ sites, $E_{ads}$ becomes −0.48, −1.02, and −1.23 eV, respectively (Table 5). For the $Sn_{5c}$-NO site, we compared the nearly vertical ($\alpha_{SnNO} = 174°$) and the tilted ($\alpha_{SnNO} = 130°$) arrangements. In the experimental study on NO adsorption on $RuO_2(110)$ [9], it was assumed that NO sits almost vertically on the $Ru_{5c}$ sites whereas on the $TiO_2(110)$ surface a tilted arrangement was predicted theoretically [10]. For $SnO_2(110)$, we find that the tilted configuration is more stable than the vertical one by 0.14 eV. The intramolecular bonding of the NO molecule is not affected much by the interaction with the surface as indicated by $R_{NO} =$ 1.15 Å, which is identical to the free gas-phase value. We also checked the influence of a symmetric adsorption of NO on both sides of the slab, which is another strategy often followed to enhance symmetry in order to save computer resources in adsorption studies. If there is charge transfer from the molecule to the surface or vice versa, artificial electrostatic interactions between the molecules on both sides of the slabs can arise. In the present case of NO adsorption on $Sn_{5c}$, this is not found as can be seen by the close agreement of the adsorption energy and structure for the one-side and two-side arrangements (Table 5). For the most stable configuration (Fig. 1), we also investigated the effect of spin polarization on the calculation of NO-surface interaction by performing a PW–GGA PAW calculation at restricted open-shell Kohn–Sham (ROKS) level. As the calculated adsorption energy, 1.18 eV, is only slightly larger than the corresponding UKS value, 1.03 eV, we assume that spin contamination does not play a significant role in the present case. This is further supported by the very small negative values of the spin density that never exceed 0.005 a.u..

The adsorption energy and geometry of the $Sn_{5c}$–NO configuration is similar to that found for $Ti_{5c}$–NO at the stoichiometric $TiO_2(110)$ surface [10]. The other configurations investigated here for $SnO_2(110)$ were not considered in that study. A weak adsorption of NO at $Ti_{5c}$ sites of the rutile (110) surface has also been found by Mguig et al. [43].

When the NO coverage is further decreased to $\theta = 0.33$, the adsorption energies are only slightly increased (by approximately 0.1 eV) compared to $\theta = 0.5$, indicating that this situation is already close to isolated molecules. For the $Sn_{5c}$-NO, $O_{2c}$-NO, and $O_{2c}$-NO-$Sn_{5c}$ sites $E_{ads}$ is −0.69, −1.14, and −1.43 eV, respectively (Table 6).

### *3.2.2 $SnO_2$(110) surface with an oxygen vacancy*

For the study of NO adsorption with oxygen vacancies present at the $SnO_2(110)$ surface, we have chosen the (2×1) and (3×1) supercell models corresponding to the removal of every second and third bridging oxygen $O_{2c}$ or in-plane oxygen $O_{3c}$, respectively, in a row. By comparing the results for the two kinds of models, we aim at modeling the situation of isolated defects. In Table 7, the defect formation energies with respect to 1/2 $O_2$ are given. Since for the isostructural $TiO_2$ rutile(110) surface the relative stability of singlet and triplet states has been discussed for the defective structures [45, 46], we computed the defect formation energy $E_{def}$ for both states. Different from $TiO_2$, where the triplet state is assumed to be the ground state or at least quasi-degenerate with the singlet state [47], there is a clear preference for the singlet state in $SnO_2(110)$ (Table 7). This is in line with the main group character of tin. Different from titanium, on tin there are no low-lying empty *d* orbitals that can take up extra electrons and form localized spin states. This observation holds

**Table 8** NO adsorption at the oxygen-defective $SnO_2(110)$ surface; adsorption energies $E_{ads}$ (eV) and geometries $R$, $\alpha$, $\phi$[a] (Å, degrees); VASP PAW UPW-GGA results; the labels correspond to Fig. 2

| Defect site | Adsorption site | Orientation | Supercell | $E_{ads}$ | Geometry |
|---|---|---|---|---|---|
| $O_{2c}$ | $O_{2c}$ | NO (a) | 2×1×3 | −1.59 | $R_{NO} = 1.23$, $R_{SnN} = 2.22$, $\phi_{NO} = 61$ |
| | | | 3×1×3 | −1.78 | $R_{NO} = 1.27$, $R_{SnN} = 2.20$, $\phi_{NO} = 70$ |
| $O_{2c}$ | $O_{2c}$ | ON (b) | 2×1×3 | −1.12 | $R_{NO} = 1.30$, $R_{SnO} = 2.32$, $\alpha_{SnNO} = 109$ |
| | | | 3×1×3 | −1.40 | $R_{NO} = 1.28$, $R_{SnO} = 2.35$, $\alpha_{SnNO} = 109$ |
| $O_{2c}$ | $Sn_{5c}$ | NO | 2×1×3 | −0.64 | $R_{NO} = 1.18$, $R_{SnN} = 2.32$, $\alpha_{SnNO} = 120$ |
| | | | 3×1×3 | −1.12 | $R_{NO} = 1.17$, $R_{SnN} = 2.34$, $\alpha_{SnNO} = 121$ |
| $O_{3c}$ | $O_{3c}$ | NO (c) | 2×1×3 | −1.16 | $R_{NO} = 1.24$, $R_{SnN} = 2.23$, $\phi_{NO} = 8$ |
| | | | 3×1×3 | −0.95 | $R_{NO} = 1.22$, $R_{SnN} = 2.24$, $\phi_{NO} = 9$ |
| $O_{3c}$ | $O_{3c}$ | ON (d) | 2×1×3 | −1.58 | $R_{NO} = 1.26$, $R_{SnO} = 2.18$, $\phi_{NO} = 72$ |
| | | | 3×1×3 | −1.43 | $R_{NO} = 1.27$, $R_{SnO} = 2.13$, $\phi_{NO} = 72$ |
| $O_{3c}$ | $Sn_{5c}$ | NO | 2×1×3 | −0.64 | $R_{NO} = 1.15$, $R_{SnN} = 2.41$, $\alpha_{SnNO} = 122$ |
| | | | 3×1×3 | −0.64 | $R_{NO} = 1.15$, $R_{SnN} = 2.40$, $\alpha_{SnNO} = 126$ |
| $O_{3c}$ | $O_{2c}$ | NO | 2×1×3 | −0.92 | $R_{NO} = 1.15$, $R_{O_{2c}N} = 1.69$, $\alpha_{O_{2c}NO} = 109$ |
| | | | 3×1×3 | −0.85 | $R_{NO} = 1.15$, $R_{O_{2c}N} = 1.74$, $\alpha_{O_{2c}NO} = 110$ |

[a] $\phi$ denotes the angle between the NO bond and the surface normal

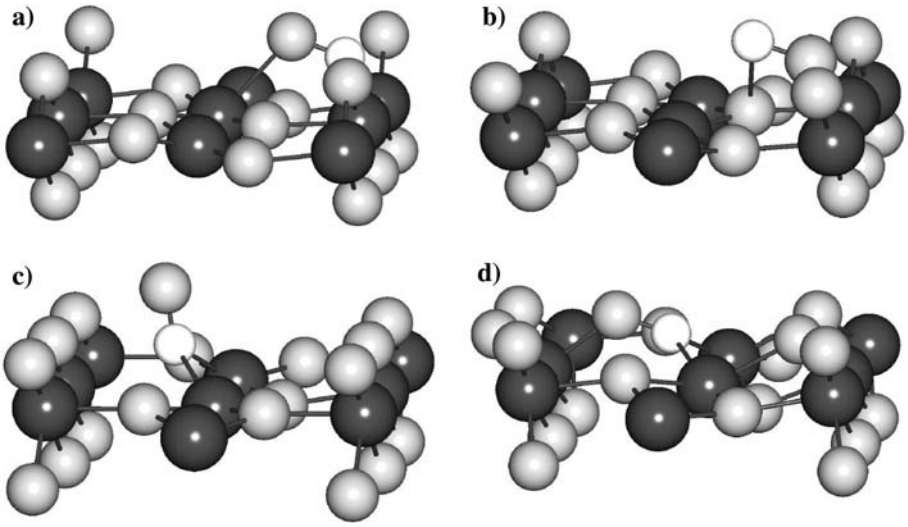


**Fig. 2** NO adsorption structures on the defective $SnO_2(110)$ surface; *white spheres*: N, *gray spheres*: O, *dark spheres*: Sn

for both $O_{2c}$ and $O_{3c}$ sites. For the formation of an $O_{2c}$ vacancy, $E_{def} = 2.95$ eV in the singlet state and $E_{def} = 3.59$ eV in the triplet state. The difference, 0.64 eV, is slightly reduced to 0.50 eV when the coverage is reduced from 0.5 to 0.33. In the light of recent investigations on the slow convergence of vacancy formation energies with decreasing coverage [46], some care has to be taken in extrapolating our present results to isolated defects. The formation of $O_{3c}$ vacancies is energetically more costly than that of $O_{2c}$ vacancies. At $\theta = 0.5$, $E_{def}(O_{3c})$ is 3.76 eV, 0.81 eV larger than for the $O_{2c}$ site. However, the difference between the vacancy formation energy of the two sites is drastically reduced, to 0.40 eV, when the concentration is decreased to 0.33 (Table 7). For this reason, we considered both defect sites in the NO adsorption study. The defect formation energies of the present study are larger by 0.4–0.6 eV than those of a previous VASP-USP study [20]. As mentioned above, this discrepancy might be due to the use of ultrasoft pseudopotentials in ref. [20].

First, we consider the adsorption of NO on the defective surface with coverage 0.5 (Table 8). The most stable adsorption sites are clearly the defect positions, shown in Fig. 2. For the $O_{2c}$ defect site, the adsorption via the N atom is preferred over the O(NO) binding mode with adsorption energies of −1.59 eV and −1.12 eV, respectively. The same observation has been made for $TiO_2(110)$ [10]. For the $O_{3c}$ defective site, the ordering is reversed. The structure with the NO oxygen replacing the previous surface oxygen site (denoted by $O_{3c}$/ON in Table 8) is more stable by 0.42 eV than the N-down structure ($O_{3c}$/NO) (Table 8). However, for this site in particular the ON adsorption causes a substantial reconstruction of the $SnO_2(110)$ surface so that the final structure is more similar to an NO bridging two $Sn_{5c}$ atoms (Fig. 2d). Different from what has been found for $TiO_2(110)$ [10], the presence of an oxygen defect has only a very small effect on the adsorption energy at the metal site (Fig. 2a). For both $O_{2c}$ and $O_{3c}$ vacancies, the $Sn_{5c}$–NO interaction energy is −0.64 eV, which is

**Table 9** Atomic spin densities based on a Mulliken analysis of the crystalline orbitals of a $2 \times 1 \times 3$ slab model obtained with CRYSTAL03 using the UPW-GGA method; corresponding UHFPW results are given in parentheses

| Adsorption site | Center | | | |
|---|---|---|---|---|
| | N(NO) | O(NO) | $Sn_{5c}$ | $O_{2c}$ |
| Stoichiometric surface | | | | |
| NO-$Sn_{5c}$ (1b) | 0.45 (0.48) | 0.38 (0.39) | 0.08 (0.02) | 0.06 (0.10) |
| NO-$O_{2c}$ (1c) | 0.42 (0.57) | 0.18 (0.25) | 0.26 (0.16) | 0.00 (0.00) |
| NO-$O_{2c}$,$Sn_{5c}$ (1d) | 0.57 (0.60) | 0.21 (0.28) | 0.15 (0.08) | 0.00 (0.05) |
| $O_{2c}$ vacancy defect | | | | |
| NO-$O_{2c}$ (2a) | 0.56 (0.42) | 0.40 (0.44) | 0.01 (0.05) | 0.06 (0.08) |
| ON-$O_{2c}$ (2b) | 0.95 (0.97) | 0.01 (0.02) | 0.00 (0.02) | 0.00 (0.00) |
| $O_{3c}$ vacancy defect | | | | |
| NO-$O_{3c}$ (2c) | 0.25 (0.39) | 0.53 (0.43) | 0.00 (0.00) | 0.10 (0.21) |
| ON-$O_{3c}$ (2d) | 0.76 (0.84) | 0.05 (0.08) | 0.00 (0.05) | 0.12 (0.05) |

only 0.02 eV larger than for the non-defective surface. For $TiO_2$(110), a dramatic increase from 0.35 eV to 0.82 eV has been found instead [10]. Again, this shows the difference in the electronic nature of Sn and Ti. In the transition metal Ti, the 3*d* population following the oxygen defect formation ($Ti^{3+}$) leads to a direct covalent bond involving the two unpaired electrons. This is not possible for the main group element Sn. For NO adsorption at a neighboring bridging $O_{2c}$ oxygen (Fig. 2b), the adsorption energy for the defective surface, −0.92 eV, is even smaller than for the non-defective surface, −1.02 eV.

The same trend is observed for the smaller coverage, $\theta = 0.33$ (Table 8). Here, the adsorption energy for N-down NO on an $O_{3c}$ vacancy site is −1.78 eV, the strongest interaction found in the present study. The O-down adsorption at this site is less stable by 0.38 eV. Again, the reverse ordering is observed for the $O_{3c}$ vacancy, the structure (2d) being more stable by 0.48 eV than structure (2c). Similar as for $\theta = 0.5$, the adsorption at the $Sn_{5c}$ site is not affected and the adsorption at the neighboring $O_{2c}$ is even destabilized.

### 3.3 Analysis of the spin distribution

The spin distribution after NO adsorption was analyzed by means of complementary CRYSTAL03 calculations at PW–GGA level. For the description of the open-shell doublet states, the unrestricted Kohn–Sham (UKS) method was used. The localized atomic basis sets as described above were used, and the spin density was calculated with the Mulliken analysis. This approach is more convenient than an a posteriori analysis of the plane-wave-based crystalline orbitals obtained with VASP. Due to the similarity of the energetic and geometric properties obtained with VASP and CRYSTAL03 for the $SnO_2$ bulk and surface (Tables 2 and 3) at the same PW–GGA level, it is assumed that the electron density is similarly described with the two approaches. In order to investigate the effect of the exchange description on the spin distribution, we also analyzed the wave functions obtained with the HFPW hybrid method. This approach is available only with CRYSTAL03.

The most stable NO adsorption geometries at the perfect and defective $SnO_2$(110) surface, as obtained with VASP for a coverage $\theta = 0.5$ ($2 \times 1 \times 3$ supercell), were considered. The surface and adsorbate geometries were taken from the VASP results. The results are summarized in Table 9. After NO adsorption at the stoichiometric surface, the largest spin density is found at the N atom of the molecule. This is obtained with both PW–GGA and HFPW methods. The spin density at the oxygen atom of NO, O(NO), and at the nearest surface atoms, $Sn_{5c}$ in the surface plane and bridging $O_{2c}$, are significantly smaller. This is particularly true for the adsorption at the $Sn_{5c}$ site, while the spin density at the surface atoms is slightly larger for the two other configurations, NO–$O_{2c}$ and NO–$O_{2c}$,$Sn_{5c}$.

For the most stable structures at the oxygen-deficient surface, the unpaired electron is localized at the NO molecule, and almost no transfer to the surface is observed. In all cases except the N-down adsorption at the $O_{2c}$ vacancy position, NO–$O_{2c}$, the spin density is smaller at the atom that replaces the missing surface oxygen than at the other atom that points away from the surface. This effect can be explained with the different coordination of the two atoms. The singly coordinated atom has the tendency to form a 'dangling bond'. In the case of N-down adsorption at the $O_{2c}$ vacancy site, the spin density is similar for the two atoms of NO.

Again, the same trends for spin localization are obtained with the two different methods, PW–GGA and HFPW. This is different from the situation at transition metal oxides like NiO, where a strong dependence of the calculated spin distribution from the exchange-correlation functional has been found [48,49]. Different from the transition metal Ni, the main-group element Sn in $SnO_2$ is not capable of stabilizing additional electrons after adsorption.

## 4 Conclusions

Energetic and structural properties of the bulk and the most stable (110) surface of tin dioxide $SnO_2$ were calculated with periodic models at the density-functional level using the Perdew-Wang exchange-correlation functional. At this level, calculations with atom-centered basis functions and with a plane-wave basis give similar results for binding energies, lattice parameters, surface relaxation, surface energy, and the formation energy of isolated oxygen surface defects. The same method was used for the description of NO adsorption at the stoichiometric and oxygen-deficient $SnO_2$(110) surface. At the regular surface, the most stable NO adsorption site is a position bridging a twofold coordinated surface oxygen and a fivefold coordinated tin atom with the formation of a O–N–O bond. The NO-surface interaction is mainly covalent and no reduction in $SnO_2$ is observed. The interaction strength of NO with the $SnO_2$(110) surface is significantly increased by the presence of oxygen defects. In these cases, an atom of the NO molecule replaces the surface oxygen at the defect position.

**Acknowledgements** T.B. thanks the Alexander von Humboldt foundation for financial support via the Feodor Lynen Postcontact Program. The work of G.P. is supported by the Italian Ministry of University and Research through a Cofin03 project.

## References

1. Batzill M, Katsiev K, Diebold U (2003) Surf Sci 529:295
2. Henrich VE, Cox PA (1994) The surface science of metal oxides. Cambridge University Press, Cambridge
3. Fayat J, Castro MS (2003) J Eur Ceram Soc 23:1585
4. Liu ZQ, Ma J, Zhang ZL, Yang XY (2003) Catal Lett 86:87
5. Ruhland B, Becker T, Müller G (1998) Sensors Actuat B 50:85
6. Leblanc E, Perier-Camby L, Thomas G, Gibert R, Primet M, Gelin P (2000) Sensors Actuat B 62:67
7. Akiyama M, Tamaki J, Miura N, Yamazoe N (1996) Denki Kagaku 64:1285
8. Abee MW, Cox DF (2002) Surf Sci 520:65
9. Wang Y, Jacobi K, Ertl G (2003) J Phys Chem B 107:13918
10. Sorescu DC, Yates JT Jr (2002) J Phys Chem B 106:6199
11. Manassidis I, Goniakowski J, Kontorovich LN, Gillan MJ (1995) Surf Sci 339:258
12. Goniakowski J, Holender JM, Kantorovich LN, Gillan MJ, White JA (1996) Phys Rev B 53:957
13. Goniakowski J, Gillan MJ (1996) Surf Sci 350:145
14. Calatayud M, Andrés J, Beltrán A (1999) Surf Sci 430:213
15. Rantala TT, Rantala TS, Lantto V (1999) Surf Sci 420:103
16. Rantala TT, Rantala TS, Lantto V (2000) Mater Sci Semicond Process 3:103
17. Mäki-Jaskari MA, Rantala TT (2001) Phys Rev B 64:075407
18. Mäki-Jaskari MA, Rantala TT (2002) Phys Rev B 65:245428
19. Melle-Franco M, Pacchioni G (2000) Surf Sci 461:54
20. Oviedo J, Gillan MJ (2000) Surf Sci 463:93
21. Oviedo J, Gillan MJ (2000) Surf Sci 467:35
22. Oviedo J, Gillan MJ (2001) Surf Sci 490:221
23. Oviedo J, Gillan MJ (2002) Surf Sci 513:26
24. Sensato FR, Custódio R, Calatayud M, Beltrán A, Andrés J, Sambrano JR, Longo E (2002) Surf Sci 511:408
25. Bates SP (2002) Surf Sci 512:29
26. Kresse G, Furthmüller J (1996) Phys Rev B 54:11169; http://cms.mpi.univie.ac.at/CMSPage/main/
27. Vanderbilt D (1990) Phys Rev B 41:7892
28. Blöchl PE (1994) Phys Rev B 50:17953
29. Kresse G, Joubert D (1999) Phys Rev B 59:1758
30. Saunders VR, Dovesi R, Roetti C, Orlando R, Zicovich-Wilson CM, Harrison NM (2003) CRYSTAL03 Users Manual, University of Torino, Torino, www.crystal.unito.it
31. Hay PJ, Wadt WR (1985) J Chem Phys 82:299
32. Check CE, Faust TO, Bailey JM, Wright BJ, Gilbert TM, Sunderlin LS (2001) J Phys Chem A 105:8111
33. Towler MD, Allan NL, Harrison NM, Saunders VR, Mackrodt WC, Aprà E (1994) Phys Rev B 50:5041
34. Perdew JP, Wang Y (1992) Phys Rev B 45:13244
35. Bredow T, Gerson AR (2000) Phys Rev B 61:5194
36. Haines J, Leger JM (1997) Phys Rev B 55:11144
37. NIST Chemistry WebBook (2003) In: Linstrom PJ, Mallard WG (eds) NIST standard reference database number vol. 69, http://webbook.nist.gov/chemistry/
38. Ramamoorthy M, Vanderbilt D, King-Smith RD (1994) Phys Rev B 49:16721
39. Bates SP, Kresse G, Gillan MJ (1997) Surf Sci 385:386
40. Elliott SD, Bates SP (2001) Phys Chem Chem Phys 3:1954
41. Bredow T, Giordano L, Cinquini F, Pacchioni G, (2004) Phys Rev B 70:035419
42. Diebold U (2003) Surf Sci Rep 48:53
43. Mguig B, Calatayud M, Minot C (2003) Surf Rev Lett 10:175
44. Duarte HA, Proynov E, Salahub DR (1998) J Chem Phys 109:26
45. Bredow T, Pacchioni G (2002) Chem Phys Lett 355:417
46. Rasmussen MD, Molina LM, Hammer B (2004) J Chem Phys 120:988
47. Lindan PJD, Harrison NM, Gillan MJ, White JA (1997) Phys Rev B 55:15919
48. Pacchioni G, Di Valentin C, Dominguez-Ariza D, Illas F, Bredow T, Klüner T, Staemmler V (2004) J Phys Condens Mat 16:S2497
49. Dominguez-Ariza D, Illas F, Bredow T, Di Valentin C, Pacchioni G (2003) Mol Phys 101:241